Published online 7 February 2017 *Nucleic Acids Research, 2017, Vol. 45, No. 8* ***4507–4518***
doi: 10.1093/nar/gkx084

Architectural plasticity of human BRCA2–RAD51 complexes in DNA break repair

Humberto Sánchez[1,*], Maarten W. Paul[2,3], Małgorzata Grosbart[1], Sarah E. van Rossum-Fikkert[1,4], Joyce H. G. Lebbink[1,4], Roland Kanaar[1,4], Adriaan B. Houtsmuller[2,3] and Claire Wyman[1,4,*]

[1]Department of Molecular Genetics, Cancer Genomics Center Netherlands, Erasmus University Medical Center, 3000 CA Rotterdam, The Netherlands, [2]Erasmus Optical Imaging Centre, Erasmus University Medical Center, 3000 CA Rotterdam, The Netherlands, [3]Department of Pathology, Erasmus University Medical Center, 3000 CA Rotterdam, The Netherlands and [4]Department of Radiation Oncology, Erasmus University Medical Center, 3000 CA Rotterdam, The Netherlands

Received October 26, 2016; Revised January 09, 2017; Editorial Decision January 27, 2017; Accepted February 03, 2017

ABSTRACT

The tumor suppressor BRCA2 is a large multifunctional protein mutated in 50–60% of familial breast cancers. BRCA2 interacts with many partners and includes multiple regions with potentially disordered structure. In homology directed DNA repair BRCA2 delivers RAD51 to DNA resulting in removal of RPA and assembly of a RAD51 nucleoprotein filament. Dynamic rearrangements of BRCA2 likely drive this molecular hand-off initiating DNA strand exchange. We show human BRCA2 forms oligomers which can have an extended shape. Scanning force microscopy and quantitative single molecule fluorescence define the variety of BRCA2 complexes, reveal dramatic rearrangements upon RAD51 binding and the loading of RAD51 patches on single strand DNA. At sites of repair in cell nuclei, super-resolution microscopy shows BRCA2 and RAD51 arranged in largely separate locations. We identified dynamic structural transitions in BRCA2 complexes suggested to facilitate loading of RAD51 onto RPA coated single strand DNA and subsequent release of BRCA2.

INTRODUCTION

Many proteins with regulatory roles, such as tumor suppressors like BRCA2, have regions of undefined structure sometimes described as intrinsically disordered. Not surprisingly due to its size and potentially disordered regions, the structure of the BRCA2 protein has been challenging researchers for more than two decades. Structural models obtained by X-ray crystallography have been determined for isolated parts of BRCA2. The DNA binding domain co-purified with the DSS1 (deleted in split-hand/split foot syndrome) protein and the BRC4 repeat fused with RAD51 show details of the interfaces between parts of BRCA2 and elements of the DNA recombination machinery (1,2). Full length BRCA2 interacts with 5–6 RAD51 molecules (3) and facilitates formation of RAD51 filaments on DNA to catalyze the strand exchange step of homologous recombination (HR) (3–5). The arrangement of BRCA2 dimers associated with RAD51 and single stranded DNA (ssDNA) has been determined from electron microscopy (EM) image reconstruction (6). BRCA2 associates with several additional partners including PALB2 that mediates interaction with BRCA1 (7,8). BRCA2 function will require dynamic rearrangement of these molecular complexes facilitating partner exchange throughout the process of HR.

Here, we investigate the global arrangement of BRCA2, changes upon RAD51 binding and loading on DNA using single-molecule visualization techniques *in vivo* and *in vitro*. Scanning force microscopy (SFM) reveals 3D structures of biomolecules *in vitro* in conditions compatible with biochemical activity. Combining SFM with total internal reflection fluorescence microscopy (TIRF-SFM) (9) allows the identification and quantification of proteins in heterogeneous mixtures like the BRCA2–RAD51 complexes addressed here. In cells, BRCA2 moves in the nucleus as oligomeric clusters together with RAD51 (10). Using single molecule localization by direct stochastic optical reconstruction microscopy (dSTORM) (11), we determined the arrangement of BRCA2, RAD51 and RPA in microscopically discernable structures (foci) formed in the cell nucleus after DNA damage induction. Although diffusing to-

*To whom correspondence should be addressed. Email: h.sanchez@tudelft.nl
Correspondence may also be addressed to Claire Wyman. Tel: +31 10 704 4337; Fax: +31 10 704 4743; Email: c.wyman@erasmusmc.nl
Present address: Humberto Sánchez, Department of Bionanoscience, Kavli Institute of Nanoscience, Faculty of Applied Sciences, Delft University of Technology, 2629 HZ Delft, The Netherlands.

gether, as reported previously (10), BRCA2 and RAD51 were largely separated at sites of DNA repair, in patterns that changed over time. These results reveal biological functions of the BRCA2 protein machinery manifest as the structural transitions and dynamic interactions observed by single molecule imaging of biochemical samples and super resolution in cells.

MATERIALS AND METHODS

Proteins, DNAs and bulk assays

BRCA2 tagged with two tandem repeats of the maltose binding protein (MBP) at the N-terminus was purified after transient transfection of human embryonic kidney 293T cells with phCMV1 plasmid containing the full length BRCA2 gene (kindly provided by S. Kowalczykowski) as described (3). Aliquots of BRCA2 with concentration range 50–100 ng/ml (as estimated using extinction coefficient at 280 nm of 365 160 M^{-1} cm^{-1}) were stored at −80°C in elution buffer from the final purification column (50 mM HEPES [pH 8.2], 10% glycerol, 450 mM NaCl, 1 mM DTT, 0.5 mM EDTA). Protein identity was confirmed by mass spectrometry (ErasmusMC Proteomics) and Western blotting (see below). BRCA2 protein was purified by three different persons in the laboratory producing four distinct stocks used for the SFM characterization. Prediction of intrinsic disordered regions in primary sequence was done using two different prediction web tools: IUpred (http://iupred.enzim.hu) (12,13) and DisEMBLTM http://dis.embl.de).

Human RAD51 and RPA were expressed in *Escherichia coli* and purified as described (14,15). RAD51 with a single cysteine exposed to the solvent was Alexa Fluor 488 (Invitrogen) labeled (degree of labeling 1.3) using maleimide chemistry and checked for biochemical activities (ATPase and D-loop formation) as described (15,16).

Escherichia coli RNA polymerase (Boehringer Mannheim) was used as SFM size calibration standard.

Linear ssDNA (1000 bases) molecules were generated by PCR amplification of pBluescript DNA and degradation of one strand with lambda exonuclease I as described (9). Circular ssDNA (5386 bases) ΦX174 Virion DNA was purchased from New England Biolabs. Oligonucleotide sequence of the 66-mer was as described (17).

Electrophoretic mobility shift assays (EMSAs) were done by mixing Cy5-labeled 90 nt ssDNA (18) (90 nM in nt) with or without RPA (60 nM) in reaction buffer (50 mM Tris–HCl [pH 7.5], 1 mM DTT, 60 mM KCl, 2 mM $CaCl_2$ and 1 mM ATP) for 10 min at 37°C in a final volume of 10 μl. Then RAD51 (300 nM), BRCA2 (20 nM), a mixture of both, or protein storage buffer was added and incubation continued for additional 20 min. The reactions products were separated on a 5% non-denaturing polyacrylamide gel running in 0.5× TB buffer at 4°C. Gels were analyzed using a Typhoon Trio scanner exciting the dye-coupled DNA.

MBP cleavage and immunodetection of BRCA2

Purified 2× MBP-BRCA2 aliquots (∼1 μg) were incubated with 2 units of PreScission protease (GE Healthcare) or with protease storage buffer for 1 h at 4°C. Reaction mixture was split for immunodetection and SFM imaging. Samples were run on a 3–8% NuPAGE Tris-Acetate gel (LifeTechnologies), which was blotted on PVDF membrane (Immobilon) for 2 h at 4°C at 300 mA. After 1 h blocking with 5% milk, the membrane was incubated with the primary antibody Anti-BRCA2 OP95, Calbiochem, 1:2000 dilution in 1% milk and 0.1% PBS buffer) overnight at 4°C. The secondary antibody (Anti-mouse HRP, Abcam, 1:2000 dilution in 1% milk and 0.1% PBS buffer) was incubated for 2 h at room temperature. The membrane was exposed with ECL (Pierce) and imaged with an Uvitec Alliance 2.7 instrument (Cambridge, UK). Cellular extracts from human BRO-derived melanoma cells treated for hyperthermia (a gift from H. Odijk) were used as molecular weight markers for endogenous BRCA2 identification (19). The protease reaction mixture was diluted ten times in BRCA2 storage buffer for SFM visualization in order to reduce background from protease molecules.

SFM microscopic analysis of protein and protein–DNA complexes

Samples were imaged in air at room temperature by tapping mode SFM using a Nanoscope III or Nanoscope IV (Digital Instruments). Silicon Pointprobe tips were type NHC-W, resonance frequency 310–372 kHz, from Nanosensors supplied by Veeco Instruments, Europe. Images were collected at 2 μm × 2 μm, 512 × 512 pixels, and processed only by flattening to remove background slope.

BRCA2 protein was diluted four times from the frozen stock with HEPES buffer (final composition: 10–25 ng BRCA2, 22 mM HEPES [pH 8.2], 2.5% glycerol, 112 mM NaCl, 0.25 mM DTT, 0.12 mM EDTA). After incubation at 37°C or on ice, as described in the text, 50 μM spermidine was added as binding agent and the protein deposited on freshly cleaved mica for 1 min, washed three times with MilliQ water and dried with filtered air.

The volume, length, and contour profile (width and height) measurements were done using 'SFMetrics' software tool as described (20). Measurements are reported together with associated standard deviations. The volume of each complex was normalized to *E. coli* RNA polymerase (RNAP) with a known molecular weight of 450 kDa that appeared in SFM as regular round objects. In order to characterize the shape of the complex the minimum length occupied by each complex, defined as skeleton length, was measured. The contours of V-shape domains of BRCA2 oligomers were traced manually.

Purified 2xMBP-BRCA2 protein (∼1 μg) was incubated with Anti-Maltose Binding Protein antibody (α-MBP ab9084, Abcam) (250 ng) for 50 min at 37°C. Unbound antibody was removed by size exclusion chromatography (Sepharose CL-4B, Sigma). Fractions containing BRCA2-α-MBP complexes were visualized by SFM.

Apparent persistence length (P_l) was obtained assuming a worm-like chain model for semi-flexible polymers. In two dimensions (2D), the mean square of the end-to-end distance (R) can be written as a function of the contour length

(C_l) and P_l:

$$\langle R^2 \rangle_{2D} = 4PL\left(1 - \frac{2P}{L}\left(1 - e^{-\frac{L}{2P}}\right)\right)$$

L measurements and P calculation were performed using 'Easyworm' software tool (21) from >100 complexes in each case.

Automatic peak-to-peak analysis was performed using 'peakfinder.m' MATLAB script (by Nathanael C. Yoder) and returned peaks at local maxima that were at least a half standard deviation of the sample above surrounding data and larger than the mean of the sample.

For *in situ* warming of BRCA2, mica containing the sample was placed on a Dry Block Thermostat UBD (Grant Instruments) at 37°C for 30 min.

Interactions between protein and DNA were performed in solution at the indicated concentrations before the sample was deposited on mica. When indicated sample was cross-linked with glutaraldehyde (0.12%) for 5 min at 37°C, quenched with 50 mM Tris–HCl [pH 7.5], and deposited in the presence of 10 mM Mg^{2+}. BRCA2–RAD51 elongated complex were selected based on eccentricity >0.7 (ratio of the distance between the foci of the ellipse modelling the protein complex and its major axis length).

Sample preparation for TIRF-SFM visualization

Nucleoprotein filaments were formed by incubating linear ssDNA (1000 bases, 1.5 μM) molecules with RAD51 (1 μM) in binding buffer (10 mM HEPES[pH 8.2], 60 mM KCl, 2 mM $CaCl_2$, 1 mM DTT and 1 mM ATP) (9,15). BRCA2–RAD51 complexes were formed by incubating an excess of RAD51 (0.6 μM) with BRCA2 (0.025 μM) in buffer containing 12.5 mM HEPES [pH 8.2], 4 mM Tris–HCl [pH 7.5], 3.25% glycerol, 125 mM NaCl, 65 mM KCl, 0.4 mM DTT, 0.17 mM EDTA, taking into account contributions from all protein storage buffers. This reaction buffer composition was kept constant in all subsequent incubations unless noted. After 30 min at 37°C, glutaraldehyde was added to a final concentration of 0.12%, followed by additional 5 min incubation, and quenched by adding Tris–HCl to a final concentration of 50 mM [pH 7.5]. The sample was diluted (from 1:20 to 1:200 in order to reduce fluorescent signal due to free RAD51) in deposition buffer (10 mM HEPES–KCl [pH 8.2], 10 mM Mg_2Cl) and deposited with 3 pM TransFluospheres on cleaved mica mounted on glass cover slips, as previously described (9,22,23). After 1 min, the mica surface was rinsed with MilliQ water and dried with filtered air. RAD51 loading onto DNA was also analyzed in ATP hydrolysis conditions by supplementing the filament formation reaction described above with 1 mM ATP and 2 mM Mg_2Cl (ATPase-Buffer). Circular ssDNA ΦX174 Virion DNA (2.4 μM in nt) was incubated with RPA (0.1 μM). When indicated RPA–DNA complexes where incubated with preassembled BRCA2 (0.025 μM)–RAD51 (0.6 μM) in ATPase-Buffer. Glutaraldehyde was added as indicated. Concentrations indicate final amount in the reactions. Samples were deposited for TIRF–SFM as described above and observed with a Nikon TE 2000U microscope as described (9). Scanning force microscopy was done with a NanoWizard®II scanner (JPK instruments) mounted on the fluorescence microscope (9,22,23). Correlation of fluorescence and topographic images was done with the JPK DirectOverlay™ software tool. Data analysis was performed with custom-made software written in MATLAB and available in http://cluster15.erasmusmc.nl/TIRF-SFM-scripts.

Quantification of fluorescent RAD51 monomers

The number of RAD51 monomers per complex was determined by quantification of fluorescence intensity by using the stepwise photobleaching of single fluorophores. In order to compensate for intensity variations due to differences in sample thickness, or constrains in the degrees of freedom of the fluorophore because of sample deposition on mica, a global estimation approach was used. Intensity of one fluorophore was defined per each field of view (FOV) after averaging the intensity steps in every region of interest (ROI) as follows; sequential frames (exposure time of 300 ms) from the same FOV were acquired until photobleaching of almost all fluorophores. This stack of images was used to make a maximum intensity projection (Supplementary Figure S2Ai) that creates an output image where each pixel contains the maximum value over all images in the stack at the particular pixel location (Supplementary Figure S2Aii). From each ROI the intensity trace over time was extracted from a sequence of 300 frames where only a few fluorophores remained blinking until complete bleaching. Intensity variations were estimated by a step fitting algorithm (9,24,25) (Supplementary Figure S2Aiii, iv). Step sizes smaller than background and bigger than two times the median value were discarded from the analysis. The reported number of fluorophores is the maximum intensity in the ROI divided by the mean of average step sizes for each ROI (Supplementary Figure S2Av, vi).

Stable nucleoprotein filaments with defined components were formed with RAD51 and 1000 nt ssDNA in the presence of ATP-Ca^{2+} (Supplementary Figure S2Bi). A perfectly formed RAD51 filament on this length DNA would consist of a maximum of 333 monomers (one RAD51 per 3 nucleotides) with a maximum length of 400 nm. Two-dimensional histograms in Supplementary Figure S2Bii and iii shows the varied population of filaments formed in these conditions (partially covered, fully covered, and association of more than one filament) as previously observed (9,15,26). For example, in the filaments grouped between 360 and 420 nm length, the main population (5% of the total) had a volume of 30–40 RNAP equiv., representing 365–489 RAD51 monomers and 200–300 fluorophores as estimated by optical microscopy. Taking into account that volume can be overestimated due to tip distortions (27), and fluorescence intensity underestimated because of surface–fluorophore interaction (9), our data is in reasonable agreement with the expected 333 RAD51 monomers per fully covered DNA molecule showing the consistency of our TIRF–SFM approach for protein quantification.

Cell culture (for super resolution microscopy)

U2OS cells were cultured in phenol-red free DMEM (Lonza) medium supplemented with 10% FCS, L-glutamine

and Pen-Strep. For microscopy experiments cells were cultured on 24 mm round coverslips of 1.5 thickness (170 ± 5 μm). Cells were irradiated the next day with 6 Gy of ionizing radiation using a ^{137}Cs source.

Immunostaining and sample preparation

After washing with PBS cells were fixed at the indicated time points with 2% PFA in PBS (Lonza) for 20 min, permeabilized with PBS with 0.1% Triton and blocked with PBS+ (0.5% BSA and 0.15% glycine). Primary antibodies were incubated at room temperature for two hours in PBS+. Primary antibodies used for those experiments were: anti-RAD51 (rabbit polyclonal) (28), mouse monoclonal anti-BRCA2 (OP95, Calbiochem) and mouse monoclonal anti-RPA32 (ab2175, Abcam). For single color dSTORM experiments RAD51 antibody was directly conjugated with Alexa647 using APEX Antibody Labeling Kit (Molecular Probes, Thermo Scientific). For dual color dSTORM experiments secondary antibodies were used.

After multiple washing steps with PBS with 0.1% Triton coverslips were incubated for 1 h with secondary antibodies recognizing either rabbit or mouse immunoglobin conjungated with fluorescent dyes, Alexa647 (Thermo Scientific) or Atto488 (Rockland). To avoid background of free antibodies, the samples were postfixed for 20 min with 2% PFA in PBS. 100 nm Tetraspeck beads (Life Technologies) were added to the fixed cells for channel alignment and drift correction. To perform dSTORM imaging coverslips were mounted in a coverslip holder and incubated in imaging buffer containing 25 mM MEA (Sigma), 0.5 mg/ml glucose oxidase (Sigma), 40 μg/ml catalase (Sigma), and 10% w/v glucose in Tris–HCl pH 8.0.

dSTORM imaging

Confocal and dSTORM data were acquired on a Zeiss Elyra PS1 system using a 100× 1.49 NA α Plan Apochromat objective. Confocal images were acquired using an Argon laser and 633 nm diode laser. For dSTORM 488 and 642 100 mW diode lasers were used to excite the fluorophores together with, respectively, a BP 495–575 + LP 750 or LP 655 excitation filter. Additionally, a 20 mW 405 laser was used to increase blinking during dSTORM imaging. Imaging was performed using HiLo illumination and the data was acquired using a 512 × 512 pixel Andor iXon DU 897 EMCCD camera. Per super resolution image 10 000–15 000 images were acquired with an acquisition time of 33 ms. Two color imaging was performed sequentially, first Alexa647 followed by Atto488.

dSTORM data analysis

A 2D Gaussian fitting algorithm (ZEN 2011, Carl Zeiss, Jena) was used to detect and localize the fluorescent events in the individual frames of the dSTORM movies. Overlapping fluorescent detections were discarded. Detections within a distance of 20 nm and five subsequent frames were assumed to originate from the same fluorophore and grouped together. Tetraspeck beads (100 nm) deposited on the cells before the experiment were used to correct for drift. To align the two color dSTORM images the positions of the same fiducials were used for an affine alignment. RAD51 dSTORM images were aligned, with the corresponding confocal image using a channel alignment algorithm in the ZEN2011 software. The confocal images were used to manually select the foci. Circular Regions of Interests with a 1 μm diameter around the foci were selected using Fiji/ImageJ. The localizations of these ROIs were exported using an ImageJ macro as text files and imported into R using the RStudio for further analysis (R Development Core Team, 2008). Localizations were clustered using a DBSCAN algorithm (Michael Hahsler (2015). dbscan: Density Based Clustering of Applications with Noise (DBSCAN) and Related Algorithms. R package version 0.9-6. (http://CRAN.R-project.org/package=dbscan). For a more detailed description of the methods see Supplementary Figure S5.

RESULTS

Human BRCA2 associates as oligomers

To study the architectural arrangements of BRCA2 protein, we purified full-length human BRCA2 protein fused with two maltose binding proteins (MBP) as described (3). Visualization by SFM reveals the ensemble of BRCA2 complexes and their structural variation at nm resolution after deposition in conditions compatible with biochemical activity (10 mM HEPES [pH 8.2], 112 mM NaCl) and in the absence of fixation agents. A variety of BRCA2 oligomers were evident in SFM images, as previously observed EM images from which prominent dimers were compiled for structure building (6). BRCA2 complexes appeared as a heterogeneous population of branched elongated structures (Figure 1A). SFM imaging provides an accurate representation of protein association in solution and distribution of multimeric states. (29,30) The volume and the skeleton length of individual BRCA2 protein complexes were used to estimate the number of monomers by a semi-automatic analysis routine (20). The distribution of BRCA2 complexes (Figure 1B), based on volume and skeleton length, had two main populations containing dimers, the most prominent, (1.6 ± 0.4 [SD] subunits) and likely tetramers or pentamers (4.6 ± 2.8 [SD]) with a skeleton length of 179 ± 114 (SD) and 403 ± 132 (SD) nm, respectively. Isolated monomers of BRCA2 were up to 100 nm in length (example boxed in Figure 1A). Inspection of the oligomeric complexes revealed an intriguing, recurrent protruding V-shape domain. One arm of the V was significantly shorter than the other (35 ± 5 [SD] nm versus 44 ± 6 [SD] nm from 235 analyzed complexes, $P < 0.05$ two-sample t-test). This arrangement could result from folding one BRCA2 monomer near the middle of the molecule, or an association between two different monomers in parallel or antiparallel orientation with a small offset. Antibodies recognizing the MBP tags increased the volume in the center of the complex but not to the protruding ends of the elongated structures (Figure 1C). This suggests that some of the C-terminal DNA binding domains could be protruding (see discussion). The association of BRCA2 into multimers and the arrangement of the elongated domains was independent of MBP as the

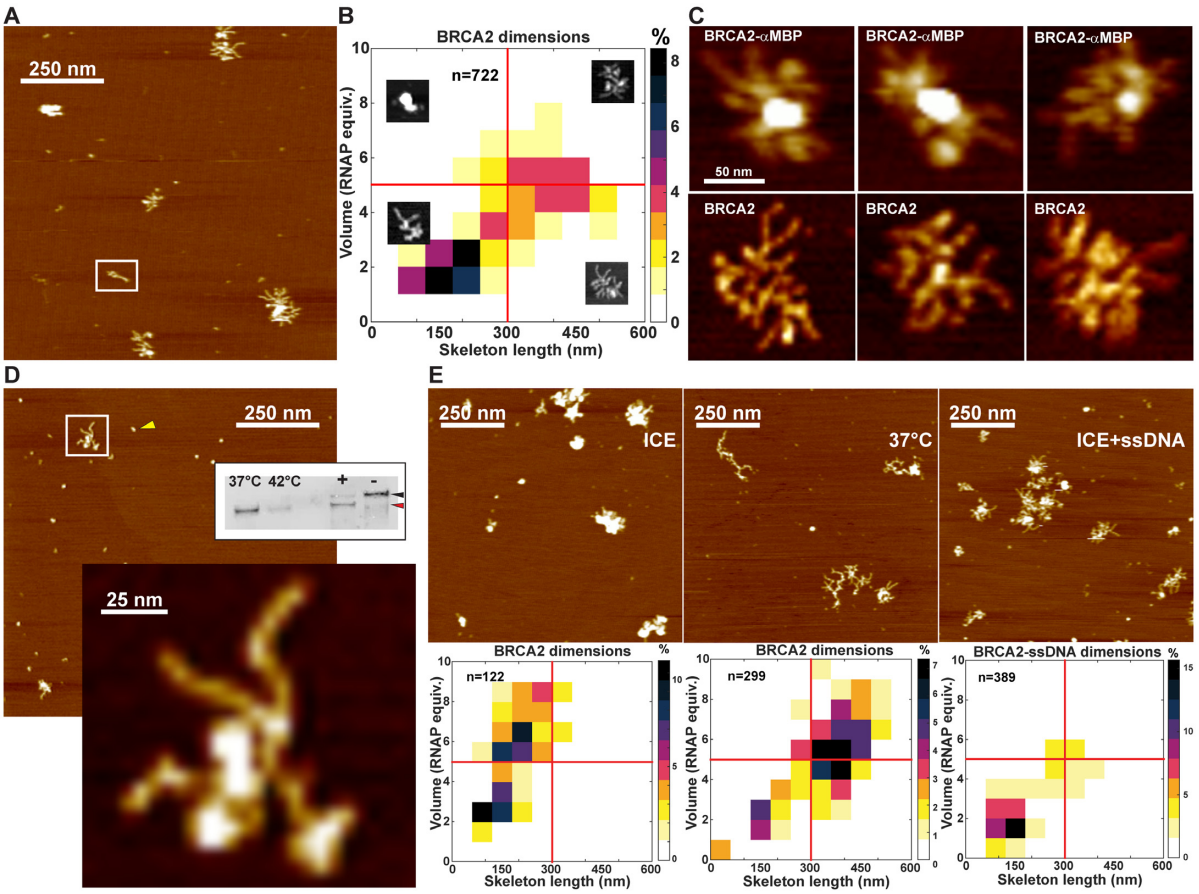

Figure 1. Human BRCA2 associates in high-order oligomers and undergoes temperature induced conformation changes. (**A**) Representative SFM image of 2xMBP–BRCA2 with several complexes from monomers (example boxed) to higher order oligomers showing a characteristic V-shape. Image size 1 × 1 μm. (**B**) Distribution of complexes based on volume and length. All individual complexes from images similar to those shown in panel A were measured and their distribution plotted in a 2D histogram with bin size 60 nm × 1 RNAP equiv. One RNAP (~450 kDa) equals approximately one 2xMBP–BRCA2 (470 kDa). Color indicates percentage of total complexes analyzed as shown in the scale bar. Red lines are guides to view bins. Inset images are zoomed examples (shown at different scales) representative of complexes in quadrants defined by the red lines. (**C**) SFM images of BRCA2 incubated with MBP antibody (upper row) compared to BRCA2 alone (bottom row). (**D**) The MBP tag does not influence BRCA2 oligomeric structure. SFM image of BRCA2 (white square and zoomed view below) after cleavage of the MBP tags by incubation with PreScission protease. The small round particles (yellow arrowhead) in the background are either protease or cleaved tag. Inset shows Western blot verification of tag cleavage. Samples are: lane '+' after and '–' before protease incubation. Western blot control and size comparison are: lane '37°C' extracts from human BRO-derived melanoma cells showing endogenous BRCA2 which is as expected degraded as shown in lane "42°C. Black arrowhead: MBP tagged BRCA2; red arrowhead: untagged BRCA2. Color intensity indicates height (from 0 to 1.5 nm, dark to light). (**E**) SFM images of BRCA2 and quantification of size distribution, in conditions as labeled; incubation on ice, *in situ* warming to 37°C, or incubation with 66 nt ssDNA.

shape or distribution of forms was unchanged after removal of the tags (Figure 1D).

The oligomeric and elongated appearance of BRCA2 suggested structural variability characteristic of proteins with intrinsically disordered regions. The structure of proteins with intrinsically disordered regions can vary dramatically due to relatively subtle change in conditions (31). We tested the effect of incubation at different temperatures and addition ssDNA on BRCA2 complex architecture. Notably, the protein complexes assumed a largely globular shape if the sample was deposited from incubation on ice (Figure 1E). This transition was readily reversible as *in situ* warming to 37°C of the sample on mica, or incubation on ice with linear ssDNA oligonucleotides before deposition for imaging, exposed the branched structures. This suggests that self-association among BRCA2 domains, resulting in globular or extended structures, is readily reversible and dynamic consistent with the behavior of intrinsically disordered regions.

Structural plasticity of human BRCA2

Primary sequence analysis predicts the frequent occurrence of segments along the BRCA2 amino acid sequence that can be described as intrinsic disordered regions (IDRs) (32,33) (Supplementary Figure S1A–C). IDRs are often characteristic of flexible linkers involved in the assembly of macromolecular complexes (33,34). We compared the dimensions of the BRCA2 elongated structures with double-stranded DNA (dsDNA) and the coiled-coils of the RAD50 component of the human MRN complex (35) visualized by SFM. Full width at high maximum (FWHM) of extended BRCA2 was similar to dsDNA or RAD50 coiled coils indicating a true width of 2 or 3 nm after accounting for SFM tip dis-

tortions (27). The apparent persistence length (PL) of elongated BRCA2 (17 ± 1 [SD] nm) was less than dsDNA (56 ± 6 [SD] nm) or RAD50 coiled coils (30 nm (36)), showing the flexibility of BRCA2 as a polymer (Supplementary Figure S1D and E).

BRCA2–RAD51 complexes are regular elongated structures

BRCA2 functions in HR associated with RAD51. To describe the arrangement and variation in BRCA2–RAD51 complexes we used TIRF-SFM (9) and compared fluorescent RAD51, hereafter RAD51 (15,16,25) (Supplementary Figure S2A), BRCA2 and a mixture of the two, in the absence of DNA and nucleotide cofactor. BRCA2–RAD51 complexes were formed at a molar ratio of 1:24 and visualized by TIRF-SFM, after fixation with glutaraldehyde (Figure 2A). In the absence of fixation limited BRCA2–RAD51 complexes were observed by SFM, indicating interactions that are dynamic or transient in these conditions. The co-incubation resulted in protein complexes with an unanticipated filament-like appearance not apparent for either RAD51 or BRCA2 separately prepared with the same fixation protocol (Supplementary Figure S3). Analysis of TIRF-SFM images revealed filament like structures ranging from 30 nm to >500 nm long, and a main population with a volume equivalent to 20–30 RNAP equiv., including 50–100 RAD51 monomers based on fluorescence (Figure 2B and C). The number of RAD51 monomers based on fluorescence intensity in BRCA2–RAD51 complexes was lower than in RAD51–DNA complexes with the same volume (see Materials and Methods and Supplementary Figure S2B for details of the quantification). The extra volume in the BRCA2–RAD51 complexes in the main population was equivalent to 12–26 BRCA2 monomers. Similar structures were observed using unlabeled RAD51 protein indicating that the regular elongated forms are not due to the fluorescent label (Supplementary Figure S4A). The elongated structures had an interrupted height profile repeating with 51 ± 67 (SD) nm periodicity along their contour, indicating the end-to-end association of smaller complexes. For comparison dimeric BRCA2–RAD51 complexes reconstructed from EM images are roughly oval at 26.5 nm × 16.5 nm (6). Additionally, BRCA2–RAD51 complexes were wider (FWHM = 17.8 ± 6 [SD] nm) and stiffer (PL = 698 ± 338 [SD] nm) than RAD51-dsDNA filaments (FWHM = 8.75 ± 3.1 [SD] nm, PL = 91 ± 11 [SD] nm) filaments (Supplementary Figure S1D). Together the volume and fluorescence analysis of complexes observed by SFM indicated they consist of 4–5 RAD51 per BRCA2, similar to the stoichiometry of on average 4.5 to maximal 6 RAD51 per BRCA2 determined by biochemical methods (3). The elongated structures indicated specific interactions, captured during fixation, resulting regular, ordered multimers with a unit length of ∼50 nm.

Multiple patches of BRCA2–RAD51 load on ssDNA

The organization of RAD51 by BRCA2, in the absence of DNA, into higher order structures larger than those previously described (6), suggested the possibility that RAD51 is loaded onto ssDNA in a manner distinct from the nucleation and growth mechanism commonly described (6,16,25,37,38). To observe the effect of BRCA2 on RAD51–DNA loading, we incubated ssDNA (ΦX174 Virion) with fluorescent RAD51 alone (Figure 3A) or with BRCA2–RAD51 (Figure 3B) in the presence of ATP and Mg^{2+}, necessary cofactors for dynamic filament assembly. We used sub-saturating concentrations of RAD51 (1 monomer per 4 nt) to highlight the possible mediator effect of BRCA2. DNA–protein complexes with fluorescent RAD51 were visualized by TIRF–SFM after fixation with glutaraldehyde (Figure 3A) and analyzed for volume and fluorescence intensity (Supplementary Figure S4B). In these conditions, RAD51 alone did not stably bind to ssDNA and the DNA appeared mainly free of protein (31 out of 37 DNA molecules, Figure 3Ai) with unbound RAD51 in the background. Incubation of BRCA2 with RAD51 resulted in multiple RAD51 patches on all ssDNA molecules (Figure 3Aii, iii). The amount of fluorescent RAD51 in these DNA-protein complexes was determined by TIRF–SFM (Supplementary Figure S4B). Volume analysis indicated that BRCA2 was included, in addition to RAD51 detected by fluorescence, in the DNA bound structures. For example, in the population with a total volume equivalent to 30–40 BRCA2 monomers and 143 ± 101 ($n = 17$) RAD51 monomers detected by fluorescence would include additional volume equivalent to 18–28 BRCA2 monomers. Both RAD51 and BRCA2 can bind ssDNA and either or both proteins could be bound in the complexes observed here. This striking association of RAD51 with DNA only in the presence of BRCA2 reflects the importance of the BRCA2–RAD51 complex for initiating DNA strand exchange.

The DNA-protein complexes observed by SFM, including RAD51 and BRCA2, had patches with regular features (Figure 3Aiii). The average length of the patches, delineated by a decrease in the cross-section height or a kink in the contour was 71 ± 24 (SD) nm (from 405 patches in 79 DNA–protein complexes). The dimensions of the DNA bound complexes (FWHM = 13.9 ± 6.7 [SD] nm, height = 3.8 ± 1.5 [SD] nm) were different from both the RAD51–dsDNA filaments (FWHM = 8.75 ± 3 [SD] nm, height = 2.5 ± 0.6 [SD] nm, $n = 101$) and the BRCA2–RAD51 complexes (FWHM = 17.8 ± 6 [SD] nm, height = 2.4 ± 0.9 [SD] nm, $n = 123$). These dimensions, together with volume measurements and number of RAD51 estimated from fluorescence, indicate that BRCA2 not only facilitates RAD51 loading on ssDNA but that interaction with ssDNA also induced partial release of BRCA2.

The apparent release of BRCA2 was more evident when the DNA protein complexes were visualized in the absence of fixation (Figure 3B). Pre-incubation of the ssDNA with RPA (visualized in Figure 3B without fixation) resulted in limited loading of RAD51 in the absence of BRCA2 (Figure 3Bii, iii and Supplementary Figure S4E and F). Interestingly, DNA electrophoretic mobility shift experiments suggest that BRCA2 could rearrange RPA on DNA (Supplementary Figure S4D, compare lanes 2 and 6). As expected, BRCA2 enhanced RAD51 loading onto RPA coated ssDNA (Figure 3B and Supplementary Figure S4E and F). About 2-fold more RAD51 was loaded onto ssDNA preincubated with RPA in the presence of BRCA2, 137 ± 42 (SD) versus 69 ± 42 (SD) RAD51 monomers per DNA molecule

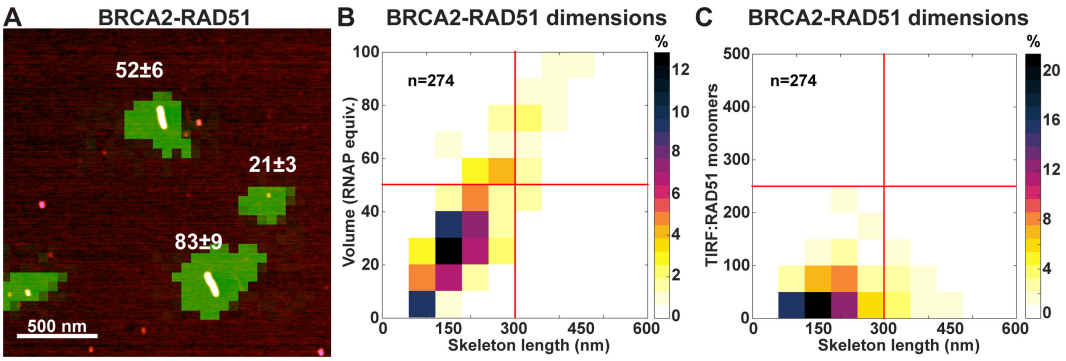

Figure 2. BRCA2–RAD51 complexes organize into filament-like structures. (**A**) RAD51–BRCA2 complexes visualized by combined SFM and fluorescence microscopy (TIRF–SFM). SFM scan overlaid with fluorescence image (green) of BRCA2 incubated with fluorescent RAD51 and cross-linked with glutaraldehyde. Numbers indicate RAD51 monomers ± SD for the complexes shown. (**B**) Volume and length of all complexes were measured and their distribution plotted in a 2D histogram with bin size 60 nm x 10 RNAP equiv. Color indicates percentage of total of complexes analyzed ($n = 274$) as shown in the scale bar. (**C**) Distribution of RAD51-BRCA2 complexes based on number of fluorophores (RAD51) and length. All complexes were measured and their distribution plotted in a 2D histogram with bin size 60 nm x 50 RAD51 monomers. Color indicates percentage of total complexes analyzed ($n = 274$) as shown in the scale bar.

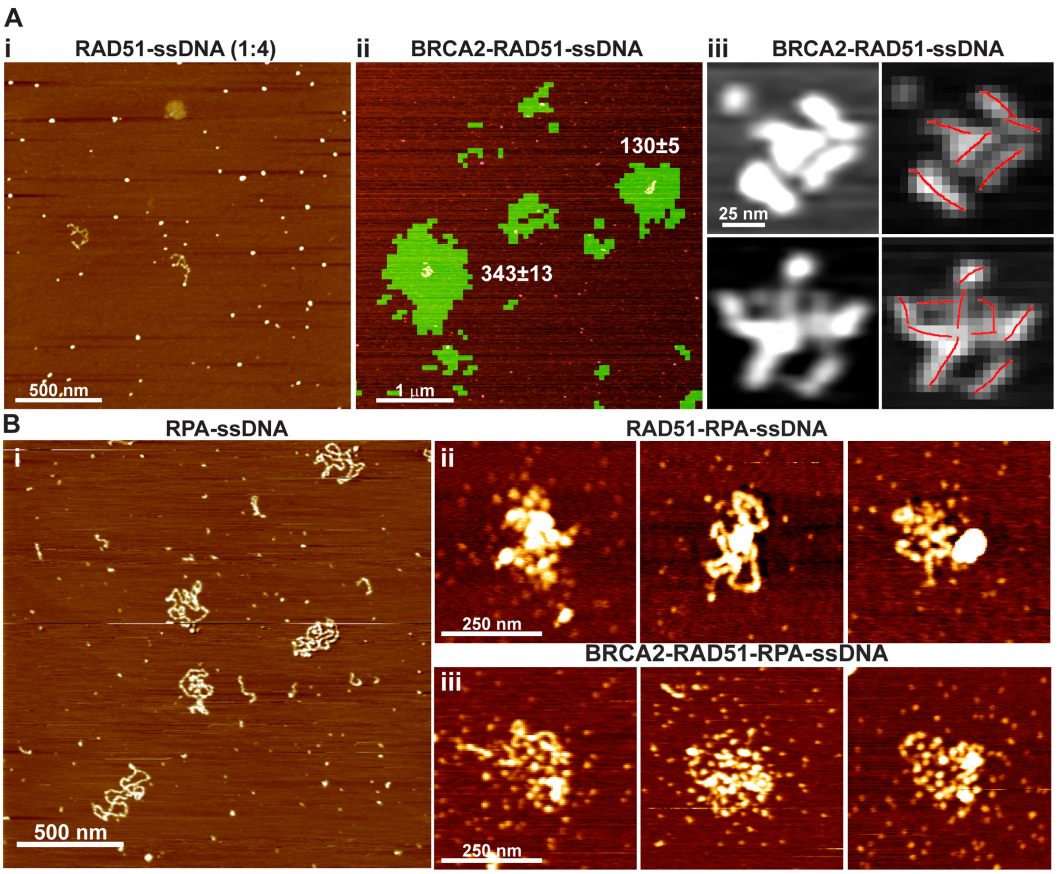

Figure 3. BRCA2 oligomers mediate RAD51 hand-off to DNA. (**A**) Loading of RAD51 on DNA (i) SFM image of ΦX174 Virion ssDNA incubated with RAD51 and cross-linked with glutaraldehyde. Color intensity indicates height (from 0 to 3 nm). (ii) TIRF-SFM image of ΦX174 Virion ssDNA incubated with BRCA2–RAD51 and cross-linked with glutaraldehyde. (iii) Examples of multiple BRCA2–RAD51 complexes bound to ΦX174 Virion ssDNA from images similar to panel B. The patch length (red line) was analyzed with 'SFMetrics'. (**B**) Loading of RAD51 on RPA coated ssDNA (i) SFM image of ΦX174 Virion ssDNA incubated with RPA, visualized without fixation. (ii) RAD51–RPA–ssDNA complexes visualized by SFM without fixation. (iii) BRCA2–RAD51–RPA–ssDNA complexes visualized by SFM without fixation.

(Supplementary Figure S4E and F). The resulting protein DNA complexes also appeared very different from those formed on ssDNA alone. BRCA2 loaded RAD51 was more evenly distributed loaded onto RPA-ssDNA, not in defined patches (compare Figure 3Aiii to Biii). In addition, based on fluorescence intensity estimates of RAD51 monomers and volume, BRCA2 was largely absent from these complexes (Figure 3B). The architectural rearrangements and molecular hand-off of RAD51 from BRCA2 to DNA was apparently enhanced by interaction with RPA.

Distinct arrangements of BRCA2 and RAD51 at DNA damage sites in the cell nucleus

With conventional microscopy resolution RAD51 and BRCA2 are reported to co-localize at sites of DNA damage (10,19,39). However, our *in vitro* results suggest that BRCA2 and RAD51 may separate once RAD51 is loaded onto DNA. To determine the arrangement of BRCA2, RAD51 and RPA in the nucleus of U2OS cells after DNA double-strand break induction, we used single molecule localization microscopy (dSTORM). This provides localization accuracy relevant to molecular dimensions. Typical accumulations of RAD51, often referred to as DNA repair foci, were clearly visible by fluorescence confocal microscopy (Supplementary Figures S5A and S6A). Localization of individual molecules by dSTORM revealed that RAD51 focal accumulations were frequently elongated some more than 400 nm long (Figure 4A–C). Subsequent two-color dSTORM imaging revealed that BRCA2 localizations were relatively diffuse with several clusters around the elongated RAD51 accumulations (Figure 4C). As expected from their relative nuclear concentration (10) and likely interaction stoichiometry (3) most BRCA2 clusters were smaller than RAD51 clusters, including fewer localizations.

The relative location of BRCA2 and RAD51 was analyzed quantitatively (Figure 4C–E, Supplementary Figure S5). Each RAD51 focus was oriented with its long axis vertical with the most intense signal up and an overlay of all foci was compiled (Figure 4E, see also Supplementary Figure S5E). BRCA2 localizations (magenta) were not concentrated in the center but clearly spread around the central RAD51 cluster. The spatial overlap between two different protein species in single molecule localization microscopy can be studied by quantifying the abundance of localizations of the one protein near localizations of the other (40). Here, the fraction of RAD51 localizations that overlapped with the BRCA2 was quantified by counting the number of BRCA2 localizations within a radius of 50 nm from every RAD51 localization (Supplementary Figure S5C and D). From this a fraction of overlapping RAD51 localizations can be calculated for every DSB focus. For each time point after DNA damage induction by ionizing irradiation (IR) we classified foci based on the fraction of overlapping BRCA2 and RAD51 they included and plotted their distribution in histograms (Figure 4D). As can be seen at all 3 time points after IR (0.5, 2 and 6 h) most foci included at least some RAD51 signal that was not overlapping with the BRCA2 signal (cumulative total of all histogram bars except fraction overlapping = 1.0). At 0.5 h after inducing breaks, with 6 Gy ionizing irradiation, the most frequent class of foci had no overlap in BRCA2 and RAD51 (30%). This pattern changed in time after irradiation. The proportion of foci with most BRCA2 and RAD51 overlapping (histogram bin at 0.8–1.0 fraction overlapping) increased at 2 and 6 h. In comparison similar two-color dSTORM imaging for RPA and RAD51 showed a different distribution within foci with varying overlap (Figure 4F, Supplementary Figure S6C and D). As a control for our imaging, analysis methods and comparison of the histogram presentations, we stained RAD51 with a mixture of secondary antibody labeled with two different dyes which showed almost complete overlap in signal, as expected (Figure 4G). We have reliably quantified the relative distribution of different proteins in DNA damage include foci, where BRCA2 and RPA were often separated from RAD51. Changes in these patterns can be correlated to dynamic interactions during the DNA repair process and used to test biological function.

DISCUSSION

We have determined the relative arrangement of essential DNA break repair proteins, BRCA2, RAD51 and RPA, in complexes on DNA from purified components and in the cell nucleus. These data identify steps in the molecular choreography of assembling functional repair machinery where it is needed. BRCA2 alone displays variable structures, depending on mild changes in conditions and to binding partners, features characteristic of proteins including intrinsically disordered regions. Binding to RAD51 induces dramatic reorganization into a regular complex capable of multimerization and active in loading RAD51 onto ssDNA. We observe at least partially release of RAD51 from BRCA2 to DNA in the presence of RPA. Super-resolution imaging in cell nuclei also indicated that BRCA2 and RAD51 separate at the sites of DNA damage. BRCA2 however remained in the area of the DNA damage, as also observed in foci with standard microscopy, possibly indicating a role late in DNA break repair.

BRCA2 is responsible for delivering RAD51 to sites of DNA breaks in the nucleus. As such it has to scan nuclear volume for sites where its action is needed. At an approximate concentration of 10 nM, in the range estimated for BRCA2 and several other DNA repair proteins in the cell nucleus (10,41,42), each protein would have to search volumes equivalent to a sphere with radius of about 300 nm. Our direct SFM visualization shows that BRCA2 oligomers can adopt an extended configuration spanning up to several hundred nanometers. BRCA2 oligomers in this conformation effectively tether multiple C-terminal DNA binding domains. In addition association with multiple RAD51 monomers effectively provides additional DNA binding domains tethered in close proximity. These features would facilitate an effective search for DNA damage sites in the nucleus via frequent non-specific interactions (10). BRCA2 regions characterized as intrinsically disordered could allow fluctuating inter- and intra-molecular associations with low entropy cost promoting conformational flexibility and functional exchange of binding partners (43). Intrinsically disordered regions of BRCA2 may also facilitate its accumulation via interaction with poly(ADP-ribose) which has been

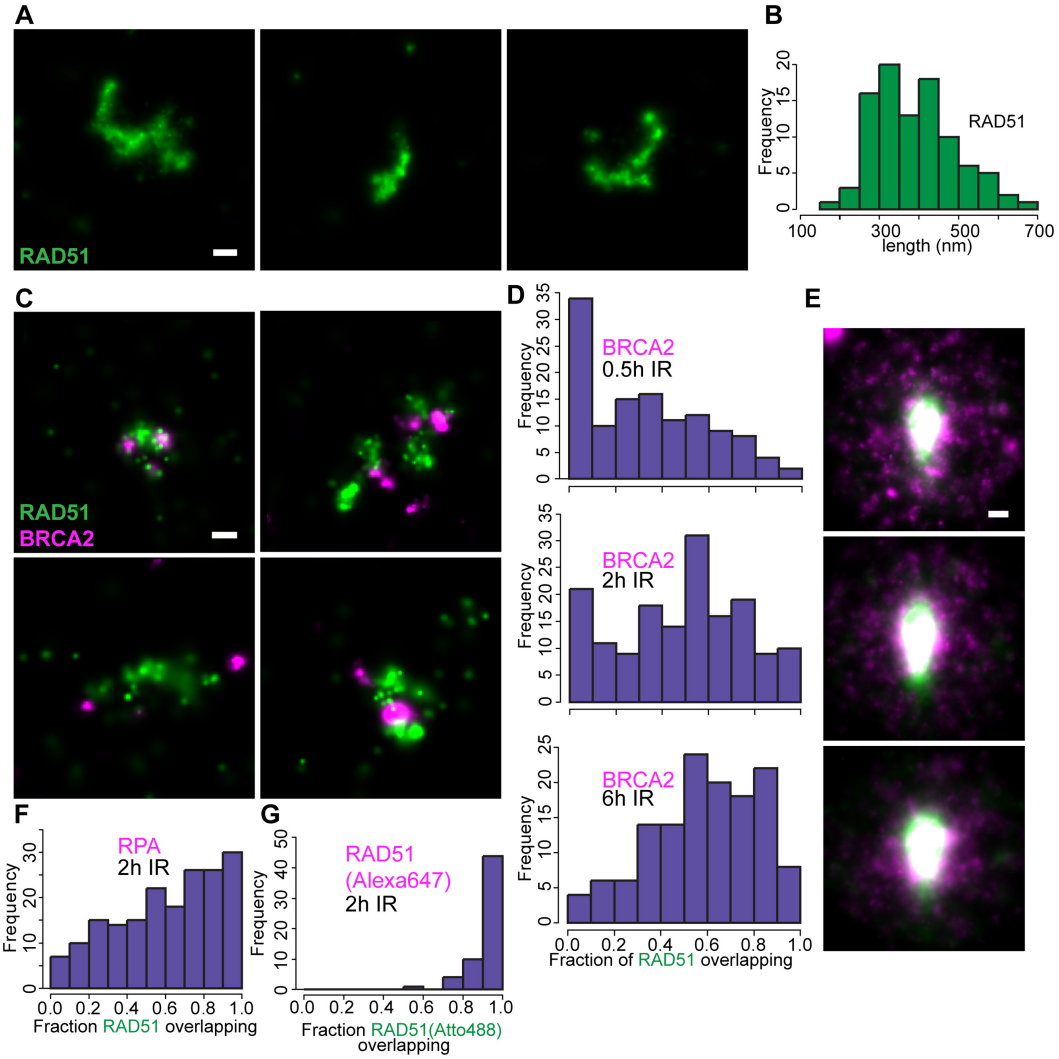

Figure 4. BRCA2 and RAD51 localize in different patterns in ionizing radiation induced foci. (**A**) Super resolution (dSTORM) images of RAD51 foci detected by immunofluorescence in U2OS cells fixed 2 h after treated with 6 Gy of ionizing radiation (IR). (**B**) Distribution of the RAD51 structures based on length of the major axis. (**C**) Examples of repair foci RAD51 (green, Atto488 conjugated secondary antibody) and BRCA2 (magenta, Alexa647 conjugated secondary antibody) acquired with dSTORM. (**D**) RAD51 localizations that overlap with BRCA2 were determined for every ROI (focus) and the distribution of foci based on fraction overlapping signals plotted in a histogram (Supplementary Figure S4D) ($n = 15, 11, 11$ cells respectively). (**E**) Summed projections of dSTORM images of repair foci aligned and rotated based on the RAD51 (green) signal, show the BRCA2 (magenta) signal spread around RAD51. Images represent the same time points as in D. (**F**) The distribution of foci based on fraction of overlapping signals for RAD51 and RPA. (**G**) As a control cells were stained for RAD51 and two different secondary antibodies showing, as expected, all foci with near complete overlap of signals in this analysis. Scale bars indicate 100 nm.

suggested to seed the accumulation of intrinsically disordered proteins at the sites of DNA breaks (44).

In vitro single-molecule experiments have extensively studied the DNA binding behavior of RAD51 (16,25,38,45) where filament formation is described as a two-steps process involving nucleation and growth. Our previous live cell imaging data (10) indicated that most, if not all, nuclear RAD51 is traveling in complex with BRCA2 suggested that filament formation in vivo may be dominated by these complexes and not free RAD51. We show here that BRCA2 transforms RAD51 into a stiff multimeric DNA binding complex offering potential mechanistic advantages. The BRCA2–RAD51 complex is essentially a multimeric DNA binding complex that would facilitate loading of RAD51 onto ssDNA in competition with proteins like RPA (3–5). Although RAD51 *in vitro* can displace RPA on ssDNA, we note that in vivo the relative concentrations of these proteins likely make this ineffective. Modification of RAD51 by phosphorylation mitigates the need for mediators to replace RPA in vitro (46). However if post-translational modification does not occur effectively until after filament formation, additional help to replace RPA initiating filament formation would be needed. Even a single BRCA2 comprising three OB folds and multiple RAD51s forms a multimeric ssDNA binding complex that we suggest could effectively compete away ssDNA-bound RPA without the need of direct interaction between BRCA2 and RPA (47). The complete dependence on BRCA2 for loading RAD51 on

ssDNA in the absence of RPA, observed here with limited RAD51 (Figure 3), possibly suggests an additional role for this complex unfolding ssDNA secondary structures. In combination BRCA2–RAD51 complexes serve a series of functions: catching RPA–ssDNA, using the BRCA2 DNA-binding domains to promote replacement of RPA for RAD51, and delivering multiple RAD51 molecules for efficient filament formation (Supplementary Figure S4G). We anticipate that the intrinsically disordered regions of BRCA2 are essential for dynamic structural rearrangements that catalyze molecular hand-off events in the cell nucleus.

Although all detectable RAD51 diffuses in the cell nucleus in complex with BRCA2 (10) release to load RAD51 onto DNA at break sites is expected in vivo. The accumulation of DNA break repair proteins at sites of damage in the cell nucleus has been extensively studied by fluorescence microscopy. After DNA breaks are induced, proteins needed to perform DNA strand exchange in HR reorganize by rapidly associating in clusters, or repair foci, in a BRCA2 dependent manner (48). The limited resolution of standard light microscopy is unable to resolve the relative arrangement of RAD51, BRCA2, and other repair proteins in foci that all appear as (overlapping) spherical clusters. The increased resolution of dSTORM, acquired by separating the fluorescence signal of individual molecules, enables accurate localization of single molecules in densely labeled samples. We present here super resolution images of RAD51, BRCA2 and RPA detected by immuno-fluorescence in DNA damage induced foci. We observe RAD51 arranged in an elongated patterns, up to several 100 nm long. Though there is no independent evidence that these structures are RAD51-DNA filaments, this elongated appearance is expected for a protein that coats DNA, in a filament. The length of the elongated RAD51 structures is reasonable given that 450 nm (approximate median of the distribution Figure 4B) is equivalent to a perfect RAD51-DNA filament including 900 nt of DNA and 300 RAD51 molecules (note number of localizations does not equal number of molecules in our super-resolution methods employing indirect immunofluorescence staining and detection of fluorophore blinking).

Our immunofluorescence experiments show distinct patterns of BRCA2, RAD51 and RPA in DNA damage induced foci. The RAD51 primary antibody used is polyclonal and will recognize many epitopes or presentations of RAD51. The monoclonal BRCA2 antibody recognizes one of the RAD51 binding BRC repeats. It is possible this epitope is not as efficiently recognized if RAD51 is bound to some of the BRC repeats in BRCA2. Even if all BRCA2 is not detected all RAD51 should be detected whereby the distinct pattern of RAD51 and BRCA2 reveal different dynamic arrangements at DNA breaks sites. At the earliest times analyzed after damage (0.5 hr) BRCA2 is in small clusters separated from most of an elongated, much larger RAD51 cluster (Figure 4D and E) consistent with a molecular hand-off upon loading RAD51 onto DNA. However, hand-off does not lead to BRCA2 absence from the foci, as BRCA2 clusters are observed also at later stages (2 and 6 h after damage induction). This suggests a role for BRCA2 beyond delivering RAD51 and that BRCA2 and RAD51 may re-associate before leaving the site of DNA damage.

In our super resolution images the RPA signal is also largely separated from RAD51 as expected if RAD51 replaces RPA bound to DNA (Figure 4F and Supplementary Figure S6C). Interestingly we observe both BRCA2 and RPA are present at the RAD51 damage induced foci at all three time points after damage induction. The retention of RPA at DSBs has been observed in yeast by ChIP, both at the DNA break site and at repair donor locus (49). We observe RPA in dense clusters, with large number of localizations, in contrast to RAD51, which is present in an extended pattern. As is the case for the DNA repair foci observed with conventional microscopy, there is no proof that the foci presented here with dSTORM represent DNA bound proteins; however their patterns are consistent with the different roles of these proteins and the structures they are expected to form on DNA.

The relative patterns of BRCA2 and RAD51 change over time after DNA damage (50). Here we observe specifically that localization of BRCA2 and RAD51 within 50 nm of each other is more common at later times, 2 and 6 hr after damage induction. At the dose of DNA damage inflicted, some of the damage is irreparable and some cells will eventually die. Thus the later time points may represent repeated attempts to repair or stalled repair. The increased association of BRCA2 and RAD51 in time may represent additional BRCA2 functions, stabilizing RAD51 association with broken DNA or more intriguingly an active role in removal of RAD51 after repair. Distinguishing these possibilities awaits further analysis and the ability to follow a repair event over time. However the ability to define and quantify relative protein arrangements demonstrates the power of our analysis to determine function in cells during the DNA repair process. We propose that the malleable nature of BRCA2, including multiple intrinsically disordered domains, facilitate its functions to locate break sites in nuclear space, exchange RPA for RAD51 on ssDNA and deliver RAD51 as multimeric complexes for efficient assembly of strand exchange machinery.

SUPPLEMENTARY DATA

Supplementary Data are available at NAR Online.

ACKNOWLEDGEMENTS

We thank I. Vidic for assistance in RPA protein purification, A. Kertokalio and R. v. Zuidam for technical assistance and D. Ristic and A. Zelensky for critical discussions and comments on the manuscript.

FUNDING

Dutch Technology Foundation (STW) project [NWO-nano11425 to C.W.]; Cancer Genomics Netherlands (NWO gravitation), Marie Curie Reintegration Grant [FP7-276898 to H.S.]; NanoNextNL, a micro and nanotechnology consortium of the Government of the Netherlands and 130 partners. Funding for open access charge: Dutch Technology Foundation.
Conflict of interest statement. None declared.

REFERENCES

1. Pellegrini,L., Yu,D.S., Lo,T., Anand,S., Lee,M., Blundell,T.L. and Venkitaraman,A.R. (2002) Insights into DNA recombination from the structure of a RAD51-BRCA2 complex. *Nature*, **420**, 287–293.
2. Yang,H.J., Jeffrey,P.D., Miller,J., Kinnucan,E., Sun,Y.T., Thoma,N.H., Zheng,N., Chen,P.L., Lee,W.H. and Pavletich,N.P. (2002) BRCA2 function in DNA binding and recombination from a BRCA2-DSS1-ssDNA structure. *Science*, **297**, 1837–1848.
3. Jensen,R.B., Carreira,A. and Kowalczykowski,S.C. (2010) Purified human BRCA2 stimulates RAD51-mediated recombination. *Nature*, **467**, U678–U662.
4. Liu,J., Doty,T., Gibson,B. and Heyer,W.D. (2010) Human BRCA2 protein promotes RAD51 filament formation on RPA-covered single-stranded DNA. *Nat. Struct. Mol. Biol.*, **17**, 1260–1262.
5. Thorslund,T., McIlwraith,M.J., Compton,S.A., Lekomtsev,S., Petronczki,M., Griffith,J.D. and West,S.C. (2010) The breast cancer tumor suppressor BRCA2 promotes the specific targeting of RAD51 to single-stranded DNA. *Nat. Struct. Mol. Biol.*, **17**, 1263–1265.
6. Shahid,T., Soroka,J., Kong,E.H., Malivert,L., McIlwraith,M.J., Pape,T., West,S.C. and Zhang,X. (2014) Structure and mechanism of action of the BRCA2 breast cancer tumor suppressor. *Nat. Struct. Mol. Biol.*, **21**, 962–968.
7. Siaud,N., Barbera,M.A., Egashira,A., Lam,I., Christ,N., Schlacher,K., Xia,B. and Jasin,M. (2011) Plasticity of BRCA2 function in homologous recombination: genetic interactions of the PALB2 and DNA binding domains. *PLoS Genet.*, **7**, e1002409.
8. Sy,S.M.H., Huen,M.S.Y. and Chen,J.J. (2009) PALB2 is an integral component of the BRCA complex required for homologous recombination repair. *Proc. Natl. Acad. Sci. U.S.A.*, **106**, 7155–7160.
9. Sanchez,H., Kertokalio,A., van Rossum-Fikkert,S., Kanaar,R. and Wyman,C. (2013) Combined optical and topographic imaging reveals different arrangements of human RAD54 with presynaptic and postsynaptic RAD51-DNA filaments. *Proc. Natl. Acad. Sci. U.S.A.*, **110**, 11385–11390.
10. Reuter,M., Zelensky,A., Smal,I., Meijering,E., van Cappellen,W.A., de Gruiter,H.M., van Belle,G.J., van Royen,M.E., Houtsmuller,A.B., Essers,J. *et al.* (2014) BRCA2 diffuses as oligomeric clusters with RAD51 and changes mobility after DNA damage in live cells. *J. Cell Biol.*, **207**, 599–613.
11. Heilemann,M., van de Linde,S., Schuttpelz,M., Kasper,R., Seefeldt,B., Mukherjee,A., Tinnefeld,P. and Sauer,M. (2008) Subdiffraction-resolution fluorescence imaging with conventional fluorescent probes. *Angew. Chem. Int. Ed. Engl.*, **47**, 6172–6176.
12. Dosztanyi,Z., Csizmok,V., Tompa,P. and Simon,I. (2005) IUPred: web server for the prediction of intrinsically unstructured regions of proteins based on estimated energy content. *Bioinformatics*, **21**, 3433–3434.
13. Fukuchi,S., Hosoda,K., Homma,K., Gojobori,T. and Nishikawa,K. (2011) Binary classification of protein molecules into intrinsically disordered and ordered segments. *BMC Struct. Biol.*, **11**, 29.
14. Henricksen,L.A., Umbricht,C.B. and Wold,M.S. (1994) Recombinant replication protein A: expression, complex formation, and functional characterization. *J. Biol. Chem.*, **269**, 11121–11132.
15. Modesti,M., Ristic,D., van der Heijden,T., Dekker,C., van Mameren,J., Peterman,E.J.G., Wuite,G.J.L., Kanaar,R. and Wyman,C. (2007) Fluorescent human RAD51 reveals multiple nucleation sites and filament segments tightly associated along a single DNA molecule. *Structure*, **15**, 599–609.
16. Candelli,A., Holthausen,J.T., Depken,M., Brouwer,I., Franker,M.A., Marchetti,M., Heller,I., Bernard,S., Garcin,E.B., Modesti,M. *et al.* (2014) Visualization and quantification of nascent RAD51 filament formation at single-monomer resolution. *Proc. Natl. Acad. Sci. U.S.A.*, **111**, 15090–15095.
17. van der Linden,E., Sanchez,H., Kinoshita,E., Kanaar,R. and Wyman,C. (2009) RAD50 and NBS1 form a stable complex functional in DNA binding and tethering. *Nucleic Acids Res.*, **37**, 1580–1588.
18. Mazin,A.V., Zaitseva,E., Sung,P. and Kowalczykowski,S.C. (2000) Tailed duplex DNA is the preferred substrate for Rad51 protein-mediated homologous pairing. *EMBO J.*, **19**, 1148–1156.
19. Krawczyk,P.M., Eppink,B., Essers,J., Stap,J., Rodermond,H., Odijk,H., Zelensky,A., van Bree,C., Stalpers,L.J., Buist,M.R. *et al.* (2011) Mild hyperthermia inhibits homologous recombination, induces BRCA2 degradation, and sensitizes cancer cells to poly (ADP-ribose) polymerase-1 inhibition. *Proc. Natl. Acad. Sci. U.S.A.*, **108**, 9851–9856.
20. Sanchez,H. and Wyman,C. (2015) SFMetrics: an analysis tool for scanning force microscopy images of biomolecules. *BMC Bioinformatics*, **16**, 27.
21. Lamour,G., Kirkegaard,J.B., Li,H., Knowles,T.P. and Gsponer,J. (2014) Easyworm: an open-source software tool to determine the mechanical properties of worm-like chains. *Source Code Biol. Med.*, **9**, 16.
22. Ristic,D., Sanchez,H. and Wyman,C. (2011) Sample preparation for SFM imaging of DNA, proteins, and DNA-protein complexes. *Methods Mol. Biol.*, **783**, 213–231.
23. Sanchez,H., Kanaar,R. and Wyman,C. (2010) Molecular recognition of DNA-protein complexes: A straightforward method combining scanning force and fluorescence microscopy. *Ultramicroscopy*, **110**, 844–851.
24. Kerssemakers,J.W., Munteanu,E.L., Laan,L., Noetzel,T.L., Janson,M.E. and Dogterom,M. (2006) Assembly dynamics of microtubules at molecular resolution. *Nature*, **442**, 709–712.
25. van Mameren,J., Modesti,M., Kanaar,R., Wyman,C., Peterman,E.J. and Wuite,G.J. (2009) Counting RAD51 proteins disassembling from nucleoprotein filaments under tension. *Nature*, **457**, 745–748.
26. Ristic,D., Modesti,M., van der Heijden,T., van Noort,J., Dekker,C., Kanaar,R. and Wyman,C. (2005) Human Rad51 filaments on double- and single-stranded DNA: correlating regular and irregular forms with recombination function. *Nucleic Acids Res.*, **33**, 3292–3302.
27. Bustamante,C., Keller,D. and Yang,G.L. (1993) Scanning force microscopy of nucleic-acids and nucleoprotein assemblies. *Curr. Opin. Struct. Biol.*, **3**, 363–372.
28. van Veelen,L.R., Cervelli,T., van de Rakt,M.W., Theil,A.F., Essers,J. and Kanaar,R. (2005) Analysis of ionizing radiation-induced foci of DNA damage repair proteins. *Mutat. Res.*, **574**, 22–33.
29. Janicijevic,A., Ristic,D. and Wyman,C. (2003) The molecular machines of DNA repair: scanning force microscopy analysis of their architecture. *J. Microsc.*, **212**, 264–272.
30. Ratcliff,G.C. and Erie,D.A. (2001) A novel single-molecule study to determine protein–protein association constants. *J. Am. Chem. Soc.*, **123**, 5632–5635.
31. Uversky,V.N. (2016) Dancing protein clouds: the strange biology and chaotic physics of intrinsically disordered proteins. *J. Biol. Chem.*, **291**, 6681–6688.
32. Cortese,M.S., Uversky,V.N. and Dunker,A.K. (2008) Intrinsic disorder in scaffold proteins: getting more from less. *Prog. Biophys. Mol. Biol.*, **98**, 85–106.
33. Oldfield,C.J. and Dunker,A.K. (2014) Intrinsically disordered proteins and intrinsically disordered protein regions. *Annu. Rev. Biochem.*, **83**, 553–584.
34. Wright,P.E. and Dyson,H.J. (2015) Intrinsically disordered proteins in cellular signalling and regulation. *Nat. Rev. Mol. Cell. Biol.*, **16**, 18–29.
35. de Jager,M., van Noort,J., van Gent,D.C., Dekker,C., Kanaar,R. and Wyman,C. (2001) Human Rad50/Mre11 is a flexible complex that can tether DNA ends. *Mol. Cell*, **8**, 1129–1135.
36. van Noort,J., van Der Heijden,T., de Jager,M., Wyman,C., Kanaar,R. and Dekker,C. (2003) The coiled-coil of the human Rad50 DNA repair protein contains specific segments of increased flexibility. *Proc. Natl. Acad. Sci. U.S.A.*, **100**, 7581–7586.
37. Holloman,W.K. (2011) Unraveling the mechanism of BRCA2 in homologous recombination. *Nat. Struct. Mol. Biol.*, **18**, 748–754.
38. van der Heijden,T., Seidel,R., Modesti,M., Kanaar,R., Wyman,C. and Dekker,C. (2007) Real-time assembly and disassembly of human RAD51 filaments on individual DNA molecules. *Nucleic Acids Res.*, **35**, 5646–5657.
39. Bekker-Jensen,S., Lukas,C., Kitagawa,R., Melander,F., Kastan,M.B., Bartek,J. and Lukas,J. (2006) Spatial organization of the mammalian genome surveillance machinery in response to DNA strand breaks. *J. Cell Biol.*, **173**, 195–206.
40. Rossy,J., Cohen,E., Gaus,K. and Owen,D.M. (2014) Method for co-cluster analysis in multichannel single-molecule localisation data. *Histochem. Cell. Biol.*, **141**, 605–612.
41. Essers,J., Hendriks,R.W., Wesoly,J., Beerens,C.E., Smit,B., Hoeijmakers,J.H., Wyman,C., Dronkert,M.L. and Kanaar,R. (2002)

Analysis of mouse Rad54 expression and its implications for homologous recombination. *DNA Repair (Amst.)*, **1**, 779–793.
42. Ghaemmaghami,S., Huh,W.K., Bower,K., Howson,R.W., Belle,A., Dephoure,N., O'Shea,E.K. and Weissman,J.S. (2003) Global analysis of protein expression in yeast. *Nature*, **425**, 737–741.
43. Shoemaker,B.A., Portman,J.J. and Wolynes,P.G. (2000) Speeding molecular recognition by using the folding funnel: the fly-casting mechanism. *Proc. Natl. Acad. Sci. U.S.A.*, **97**, 8868–8873.
44. Altmeyer,M., Neelsen,K.J., Teloni,F., Pozdnyakova,I., Pellegrino,S., Grofte,M., Rask,M.B.D., Streicher,W., Jungmichel,S., Nielsen,M.L. *et al.* (2015) Liquid demixing of intrinsically disordered proteins is seeded by poly(ADP-ribose). *Nat. Commun.*, **6**, 8088.
45. Hilario,J., Amitani,I., Baskin,R.J. and Kowalczykowski,S.C. (2009) Direct imaging of human Rad51 nucleoprotein dynamics on individual DNA molecules. *Proc. Natl. Acad. Sci. U.S.A.*, **106**, 361–368.
46. Subramanyam,S., Ismail,M., Bhattacharya,I. and Spies,M. (2016) Tyrosine phosphorylation stimulates activity of human RAD51 recombinase through altered nucleoprotein filament dynamics. *Proc. Natl. Acad. Sci. U.S.A.*, **113**, E6045–E6054.
47. Sing,C.E., Olvera de la Cruz,M. and Marko,J.F. (2014) Multiple-binding-site mechanism explains concentration-dependent unbinding rates of DNA-binding proteins. *Nucleic Acids Res.*, **42**, 3783–3791.
48. Tarsounas,M., Davies,D. and West,S.C. (2003) BRCA2-dependent and independent formation of RAD51 nuclear foci. *Oncogene*, **22**, 1115–1123.
49. Wang,X. and Haber,J.E. (2004) Role of Saccharomyces single-stranded DNA-binding protein RPA in the strand invasion step of double-strand break repair. *PLoS Biol.*, **2**, E21.
50. Essers,J., Houtsmuller,A.B., van Veelen,L., Paulusma,C., Nigg,A.L., Pastink,A., Vermeulen,W., Hoeijmakers,J.H.J. and Kanaar,R. (2002) Nuclear dynamics of RAD52 group homologous recombination proteins in response to DNA damage. *EMBO J.*, **21**, 2030–2037.